CHEMISTRY OF MATERIALS

ARTICLE

pubs.acs.org/cm

Interlayer Expansion of the Layered Zeolite Precursor RUB-39: A Universal Method To Synthesize Functionalized Microporous Silicates

Hermann Gies,*[,†] Ulrich Müller,[‡] Bilge Yilmaz,[‡] Takashi Tatsumi,[∥] Bin Xie,[§] Feng-Shou Xiao,[§,⊥] Xinhe Bao,[○] Weiping Zhang,[○] and Dirk De Vos[&]

[†]Inst. f. Geologie, Mineralogie und Geophysik, Ruhr-Universität Bochum, 44780 Bochum, Germany

[‡]BASF SE, Chemicals Research and Engineering, 67056, Ludwigshafen, Germany

[§]State Key Laboratory of Inorganic Synthesis and Preparative Chemistry, Jilin University, 130012, Changchun, People's Republic of China

[∥]Chemical Resources Laboratory, Tokyo Insitute of Technology, Yokohama, Japan

[⊥]Department of Chemistry, Zhejiang University, Hangzhou, People's Republic of China

[○]State Key Laboratory of Catalysis, Dalian Institute of Chemical Physics, Dalian, People's Republic of China

[&]Centre for Surface Chemistry and Catalysis, K. U. Leuven, Leuven, Belgium

ABSTRACT: Interlayer expansion reaction leads to a new family of microporous framework silicates using hydrous layer silicates as precursors. Using silylating agents such as dichlor-dimethylsilane (DCDMS), neighboring layers connect. In addition to the topotactic condensation of hydrous silicates, this leads to expanded silicate frameworks, with the number of pore openings increased by two Si-units. The hydrous layer silicate RUB-39 has been subjected to interlayer expansion reaction, using DCDMS at 180 °C, yielding new, crystalline microporous frameworks (COE-1 and COE-2), varying in their methyl function carrying as-made and oxidized calcined forms, respectively. An intersecting two-dimensional (2D) channel system with 10- and 12-membered rings is accessible for probe molecules, leading to a surface area of 540 m^2/g and a pore volume of 0.169 cm^3/g. The powder diagram was indexed in space group $P2$ with a = 15.609(3) Å, b = 11.163(1) Å, c = 7.301(1) Å, and β = 91.2(1)° for COE-1 and a = 15.594(4) Å, b = 11.039(2) Å, c = 7.276(1) Å, and β = 91.2(1)° for calcined COE-2. Rietveld refinement of the powder X-ray diffractometry (PXRD) diagram confirmed the framework topology for COE-1 and COE-2 (χ^2 = 8.0 and 9.9, respectively) and showed that the silicate framework suffers from stacking disorder after interlayer expansion reaction. DIFFaX simulations allowed for the modeling of the stacking disorder, showing that RRO- and HEU-type stacking occurs.

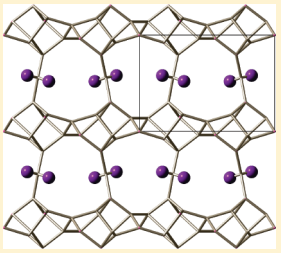

KEYWORDS: interlayer expansion, zeolite, crystal structure, IEZ-RRO, Rietveld analysis, RUB-39

INTRODUCTION

Zeolites are microporous solids that exhibit a wide range of useful properties. Their applications include the following: sorbents; ion exchangers;[1] acid,[2−5] base,[6] and oxidation catalysts;[7] in environmental applications;[4,8] and finally as carriers for highly dispersed nanoparticles.[9] Their high commercial impact was an important driving force in materials development, with the result that, today, more than 190 different microporous framework structure types are known, comprising thousands of materials with a diverse selection of compositions.[10] Despite the large variety of structures and compositions, only some of these framework structure types are in important commercial applications, and most of the materials are silicate zeolites.[11] Still, there is an intensive search for new microporous frameworks, in particular with properties tailored for specific processes. In heterogeneous catalysis, new concepts for oxidation reactions are sought, as well as more-effective catalysts for the conversion of alternative raw materials (e.g., methanol, biorenewables) to fuels and base chemicals (e.g., gasoline/diesel, olefins) and eventually to products of higher added value, such as fine chemicals.

In recent years, crystalline layered silicates have been used as precursors for the synthesis of new zeolite frameworks through a topotactic condensation reaction.[12−17] The advantage of this procedure is that the precursor can still be modified and the condensation reaction produces the calcined microporous framework in a single-step reaction. In addition to all-silica materials, Al-, B-, Fe-, Ga-, Zn-, Ti-, and Ge-substituted precursors have also been synthesized and successfully converted to silicate zeolites.[18,19] Delamination of precursors and arrangement of the delaminated particles as a "stack of cards",[20−22] or modification of the delaminated intermediate before reassembly, demonstrate different strategies that make use of the still-unfinished precursor prior to topotactic condensation, which concludes the transformation to the final state.[23−26] Recently, Tatsumi and co-workers showed a surprising new way to modify layered precursors to form crystalline microporous materials via the so-called "interlayer expansion reaction".[27−29] Treating the layered MWW or CDO precursors with dimethyldiethoxysilane under acidic conditions at ∼100 °C, the silicate layers are connected to each other via siloxane bridges opening pore space by one tetrahedral unit, as compared to the simple condensation reaction. Other than the

Received: December 9, 2010
Revised: March 31, 2011
Published: April 18, 2011

pioneering work of Kuroda et al.,[30−32] who applied similar strategies to layered silicates to obtain more or less amorphous products, these interlayer-expanded zeolites (IEZs) are crystalline and show properties that are comparable with microporous silicate zeolites. In our studies of modification of layered silicates, RUB-39[33] was used as a case study to show that the condensation product RUB-41 has unique sorption properties[34] and that the introduction of Al leads to a selective microporous acid catalyst.[35]

Conceptually, layered silicates as precursors lead to all-silica framework structures after topotactic condensation or interlayer expansion through silylation, limiting their applications to sieving and sorption properties. However, systematic studies on RUB-39 and its condensation products showed that it is possible to substitute hetero-T-atoms (such as Al, B, Ga, etc.) for Si and, thus, introduce charge on the framework of the condensation product. Structural studies showed that the active center of the zeolite framework is on a specific T-site, which should have positive impact on the selectivity of the reaction path.[33] In fact, the new materials were shown to be active acid catalysts in, e.g., amination reaction[35] with unique selectivity.

In this contribution, we report on a new system of interlayer-expanded zeolites (denoted as IEZ-RRO), showing that the concept is applicable rather generally to layered silicates, and that a wide range of silylating agents can be used to carry out the reaction. In addition, we provide a detailed structural characterization of the simplest expanded products (denoted as COE-1 and COE-2), using Rietveld analysis of powder X-ray data, DIFFAX simulations, calculations of the disorder in stacking HEU-layers during the expansion process, argon, and methane adsorption isotherms, and, finally, multinuclear solid-state nuclear magnetic resonance (NMR) experiments, confirming the interlayer expansion and the bonding state of the bridging siloxane and the role of the structure-directing agent (SDA).

EXPERIMENTAL SECTION

Synthesis of COE-1 and COE-2. Typically, 0.9 g of dichlorodimethylsilane (DCDMS) was added into 150 mL of HCl solution (0.7 M), followed by the addition of 3.0 g of pure silica RUB-39, which is a hydrous layer silicate containing dimethyl-dipropylammonium cations as charge-compensating interlayer cations. After stirring for 4 h at room temperature and ultrasonic treatment at room temperature for 2 h, the sample was transferred to an autoclave for the treatment at 180 °C for 24 h. After filtration and drying, 2.74 g of solid product, designated as COE-1, was obtained (yield of ∼91.3%). After calcination at 500 °C for 6 h, the organic groups in COE-1 were completely removed, yielding a new material, which was designated as COE-2.

Morphology of Interlayer-Expanded Materials. The morphology of the materials was studied using scanning electron microscopy (SEM). As can be seen in Figure 1, COE-2 has a sheetlike morphology that is typical for layered materials and similar to that of RUB-39, the parent material. Obviously, the interlayer expansion reaction and the subsequent calcination did not affect crystallinity and particle morphology of the synthesis product RUB-39.

NMR Spectroscopy. Solid-state NMR spectra were recorded on a Varian Infinity Plus 400 spectrometer. ^{29}Si MAS NMR spectra were acquired at 79.4 MHz, using a 7.5 mm MAS probe with a spinning rate of 4 kHz. Chemical shifts were referenced to 4,4-dimethyl-4-silapentane sulfonate sodium (DSS) at 0 ppm. The spectra were accumulated for 1024 scans with a $\pi/4$ pulse width of 1.9 μs and a recycle delay of 4 s. ^{1}H→^{13}C CP/MAS NMR spectra were recorded at 100.5 MHz and a spinning rate of 10 kHz, with a contact time of 6 ms, a recycle delay of 2 s, and 4000 scans, using a 4 mm MAS probe. The chemical shifts were referenced to adamantane with the upfield methine peak at 29.5 ppm.

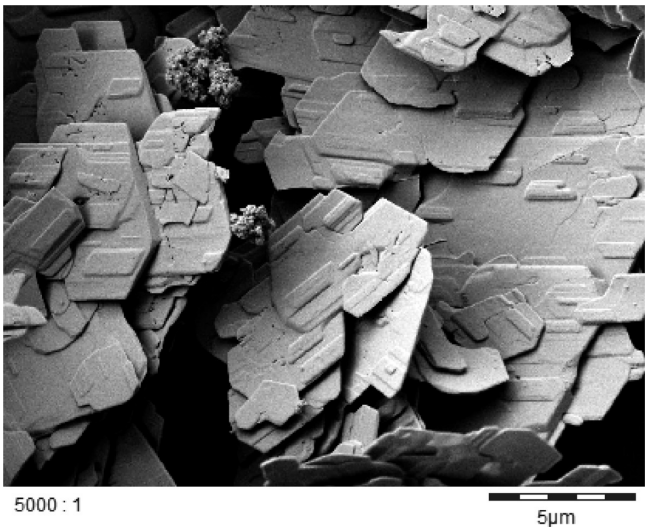

Figure 1. Scanning electron microscopy (SEM) image of COE-2 material, showing a platelike morphology similar to the parent material RUB-39, which is typical for hydrous layer silicates.

X-ray Diffraction and Structure Analysis. X-ray diffraction (XRD) analysis was carried out on as-made sample of IEZ-RRO, COE-1, as well as on the calcined sample, COE-2, of the same material. High-resolution PXRD data were collected at room temperature with a Siemens D5000 diffractometer operating in quasi Debye−Scherrer mode, using monochromatized Cu Kα_1 radiation. To prevent preferred orientation of the platelet sample transmission geometry was used with capillary sample holders. Further details of the diffraction experiment are summarized in Table 1.

Based on the indexed powder pattern, a structure model for COE-1 was derived, adapted from the layered precursor RUB-39, and energy-minimized using DLS with d(Si−O) = 1.61 Å, d((O−O) = 2.60 Å, and d(Si − Si) = 3.10 Å as constraints[36] (see Table 2). Subsequently, the coordinates of the optimized tetrahedral network were used as starting parameters for the Rietveld refinement of the PXRD data, using the Fullprof-Suite of programs[37,38] (χ^2 = 8.0 (COE-1), 9.9 (COE-2)). Inspection of the refined dataset revealed the presence of additional peaks, indicating that alternative stacking modes of layers was highly likely. Therefore, heulandite stacking of the layer (i.e., AB-stacking sequence of layers) was assigned as the other ordered end-member framework type and, using the same strategy, energy-minimized with DLS refinement. The simulated powder diagram of IEZ-HEU was then combined with that obtained from the IEZ-RRO model and compared with the experimental data. Because of the extensive number of variables involved in describing the two possible structures, parameter refinement was no longer possible. Instead, comparison of the simulated powder diagrams of the two optimized structure models with the experimental diffraction pattern was applied. A scaling factor was used to describe the relative proportion of RRO and HEU stacking, respectively. Finally, a DIFFaX model[39] of the stacking disorder of IEZ-RRO/HEU was also simulated, to show the coherence of the framework periodicity.

Similarly, the same strategy was successfully used for the calcined sample and also resulted in a satisfactory analysis of the structure describing the SDA-free framework and the oxidized bridging siloxane group, now carrying two hydroxyl groups. A summary of the optimized framework structures and the experimental parameters used in the Rietveld analysis, as well as the description of stacking disorder in the material, is shown in Tables 3−5.

Table 1. Summary of Powder X-ray Experiments and Data Analysis

sample	COE-1	COE-2
condition of data collection	room-temperature measurements	
diffractometer	Siemens D 5000	
sample holder	capillary	
wavelength	1.54056 Å (Cu $K\alpha_1$ radiation)	
2θ range	5.05°−60.00°	
step size	0.0078° 2θ	
number of points	7046	
total no. of reflections	483	
fwhm	0.156 (2θ = 14.49°)	0.187 (2θ = 14.58°)
peak profile	Thompson−Cox−Hastings pseudo-Voigt* axial divergence asymmetry	
number of distance restraints	109	
setting for restraints	d(Si−O) = 1.61(5) d(O−O) = 2.62(2) d(Si−Si) = 3.10(3)	
space group	P2 (No. 3)	
lattice parameters	a = 15.609(3) Å b = 11.163(1) Å c = 7.301(1) Å β = 91.2(1)°	a = 15.594(4) Å b = 11.039(2) Å c = 7.276(1) Å β = 91.2(1)°
number of profile parameters	8	8
number of structural parameters	125	120
residuals of refinement (conventional)		
R_p	20.1	21.2
R_{wp}	18.4	21.1
R_{exp}	6.5	6.7
χ^2	8.0	9.9
R_{Bragg}	6.8	7.5

Table 2. Parameter Settings for Structural Parameters Used for DLS Refinement

lattice parameters	values from PXRD refinement were kept fixed
space group symmetry	determined from the model, in agreement with XRD
d(Si−O)	1.62 Å
Si coordination	tetrahedral
Si−O−Si angle	145°
starting coordinates	derived from structure model refined in repetitive runs to confirm DLS minimum

Argon, Nitrogen, and Methane Adsorption. Gas adsorption experiments (Ar, N_2, and CH_4) were carried out on a Micromeritics ASAP 2420 accelerated surface area and porosimetry system. Prior to the start of the measurements, calcined samples were kept in vacuo (i.e., degas) at 473 K for 4 h. Argon sorption measurements were performed at 87 K. Median pore width, pore-size distribution, and pore volume were derived from the argon isotherm, using the Horvath−Kawazoe model. Cumulative surface area and pore volume also were calculated using the MP-method, based on the argon sorption data. Nitrogen adsorption/desorption experiments were performed at 77 K. Values for pore volume and surface area were calculated from the N_2 isotherms as well, using the *t*-plot and BET methods, respectively. Methane adsorption isotherms were recorded at two different temperatures, namely, at 298 and 313 K. Results were reported in terms of adsorbed quantity and weight percent of methane.

Table 3. Final Fractional Coordinates for IEZ-RRO after DLS Refinement[a]

	x	y	z
Si1	0	0	0
Si2	0.17988	0.92346	0.91918
Si3	0.29914	0.14310	0.99016
Si4	0.5	0.10050	0.5
Si5	0.43783	0.96360	0.15613
Si6	0.21491	0.30448	0.28390
Si7	0.32010	0.17505	0.57868
Si8	0.20062	0.95798	0.50831
Si9	0.06191	0.13914	0.34304
Si10	0.28399	0.79664	0.21374
Si11	0.24802	0.55934	0.38170
O1	0.91562	0.91609	0.00086
O2	0.99673	0.08398	0.82042
O3	0.24095	0.82372	0.01516
O4	0.17460	0.89985	0.70150
O5	0.21835	0.05510	0.95992
O6	0.32454	0.20031	0.79593
O7	0.37923	0.06964	0.07346
O8	0.27414	0.25053	0.12629
O9	0.58436	0.18454	0.50055
O10	0.50292	0.01627	0.67937
O11	0	0.91302	0
O12	0.37769	0.85690	0.22887
O13	0.21010	0.44900	0.26437
O14	0.25767	0.27211	0.48072
O15	0.12023	0.24715	0.26757
O16	0.28357	0.04195	0.54011
O17	0.22333	0.85185	0.36797
O18	0.12227	0.03571	0.42720
O19	0	0.18917	0.5
O20	0.29084	0.65311	0.24439

[a] Unit-cell parameters: a = 15.60 Å, b = 11.12 Å, c = 7.30 Å, β = 91.2°, space group *P*2, R-factor: 0.33%.

RESULTS AND DISCUSSION

The As-Made IEZ-RRO Material COE-1. RUB-39 was synthesized using procedures described in the literature. Interlayer expansion was performed with dichloro-dimethylsilane (DCDMS) under acidic conditions, using hydrothermal techniques. The morphology of the interlayer expanded product showed no changes and still resembles the layer-silicate precursor. The morphological characteristic also remained after calcination of the IEZ product at 550 °C, which leads to the removal of the methyl groups at the linking silicate units, converting them to hydroxyl groups (see Figure 1).

The ^{29}Si MAS NMR spectra of IEZ-RRO before and after calcination are shown in Figure 2. The resonances between −109 and −113 ppm are ascribed to Si atoms coordinated with four Si atoms, namely, $Si(OSi)_4$ groups (Q^4). The signal at −102 ppm is attributed to the silanols, namely, $Si(OH)(OSi)_3$ groups (Q^3). The signal at ca. −95 ppm can be assigned to the $Si(OH)_2(OSi)_2$ groups (Q^2). For the COE-1 sample before calcination (Figure 2a), there is another peak at −14 ppm, which can be assigned to the Si-CH_3 species. This indicates that the silylation occurred through the reaction of DCDMS with the silanols on the layer surface to form pillaring silicon species between the layers. Upon calcination, the peak at −14 ppm disappears, indicating that the methyl groups were replaced by the silanol groups to form more Q^2 sites connected to the adjacent layers in the COE-2 sample (see Figure 2b).

Figure 3 shows the ^{1}H →^{13}C CP/MAS NMR spectrum of IEZ-RRO, i.e., COE-1. The main peak at −1 ppm can be attributed to the

Table 4. Final Fractional Coordinates for IEZ-HEU after DLS Refinement.

	x	*y*	*z*
Si1	0	0	0
Si2	0.18161	0.96599	0.92809
Si3	0.29776	0.07697	0.99182
Si4	0.5	0.05868	0.5
Si5	0.43928	0.98893	0.15913
Si6	0.21102	0.15647	0.27980
Si7	0.31840	0.09269	0.57191
Si8	0.20224	0.98171	0.50818
Si9	0.06072	0.06976	0.34086
Si10	0.28898	0.90221	0.22020
Si11	0.17801	0.28642	0.40303
Si12	0.5	0.51094	0.5
Si13	0.67686	0.47444	0.40345
Si14	0.76237	0.60042	0.48896
Si15	0	0.57589	0
Si16	0.92134	0.52985	0.63414
Si17	0.69275	0.66549	0.82278
Si18	0.82314	0.61239	0.09655
Si19	0.73763	0.48641	0.01104
Si20	0.57866	0.55698	0.86586
Si21	0.80725	0.42133	0.67722
Si22	0.60925	0.78556	0.71034
O1	0.91467	0.95840	0.00568
O2	1.00078	0.04215	0.81957
O3	0.24543	0.91702	0.02154
O4	0.17868	0.95622	0.70839
O5	0.21615	0.03257	0.97425
O7	0.32132	0.10246	0.79160
O8	0.37910	0.04134	0.07670
O9	0.27436	0.13289	0.12233
O10	0.58533	0.10028	0.50569
O11	0.49921	0.01653	0.68043
O12	0.38060	0.93590	0.24029
O13	0.5	0.96274	0
O14	0.19733	0.22801	0.25916
O15	0.25456	0.14165	0.47844
O16	0.11939	0.12280	0.25970
O17	0.28386	0.02610	0.52575
O19	0.22563	0.92580	0.37765
O20	0.12091	0.01735	0.42330
O21	0	0.09594	0.5
O22	0.30269	0.83064	0.24089
O23	0.16301	0.35228	0.33431
O25	0.42701	0.46919	0.59086
O26	0.45576	0.55315	0.34467
O27	0.71968	0.43078	0.55708
O28	0.71008	0.45575	0.20233
O29	0.70341	0.54271	0.44630
O30	0.60189	0.63108	0.29767
O31	0.84781	0.57996	0.60189
O32	0.70953	0.64777	0.61110
O33	0.07298	0.61763	0.90914
O34	0.04424	0.53368	0.15533
O35	0.88159	0.46396	0.59617
O36	0	0.54273	0.5
O37	0.66293	0.73473	0.83434
O38	0.78032	0.65605	0.94292
O39	0.61841	0.62287	0.90383
O40	0.79659	0.54412	0.05370
O42	0.79047	0.43906	0.88890
O43	0.65219	0.50687	0.89811
O44	0.5	0.54410	0

[a] Unit-cell parameters: *a* = 5.60 Å, *b* = 22.40 Å, *c* = 7.30 Å, ss = 91.2°, space group *P*2; R-factor: 0.25%.

Table 5. Fractional Coordinates of Atoms (COE-1) with Site Occupancy Factors of the IEZ-RRO Silicate Framework after Rietveld Analysis

framework atom	*x*	*y*	*z*	site occupancy factor, SOF
Si1	0	0.038(7)	0	0.5
Si2	0.185(2)	0.956(4)	0.922(5)	1.0
Si3	0.318(3)	0.154(3)	0.015(5)	1.0
Si4	0.5	0.088(6)	0.5	0.5
Si5	0.442(3)	0.954(4)	0.149(6)	1.0
Si6	0.226(3)	0.319(3)	0.287(6)	1.0
Si7	0.321(2)	0.185(4)	0.596(6)	1.0
Si8	0.203(3)	0.972(3)	0.500(5)	1.0
Si9	0.069(3)	0.158(4)	0.363(6)	1.0
Si10	0.280(2)	0.802(3)	0.212(6)	1.0
Si11	0.173(6)	0.583(3)	0.332(19)	1.0
O1	0.924(4)	0.949(6)	0.037(12)	1.0
O2	0.978(5)	0.123(7)	0.832(10)	1.0
O3	0.226(5)	0.846(7)	0.031(8)	1.0
O4	0.193(5)	0.933(7)	0.716(6)	1.0
O5	0.219(4)	0.076(6)	0.999(11)	1.0
O6	0.326(5)	0.199(7)	0.807(6)	1.0
O7	0.385(4)	0.072(6)	0.081(11)	1.0
O8	0.289(5)	0.263(6)	0.146(9)	1.0
O9	0.570(4)	0.178(6)	0.466(12)	1.0
O10	0.514(5)	−0.010(6)	0.651(10)	1.0
O11	0.5	0.915(9)	0	0.5
O12	0.373(4)	0.853(7)	0.205(11)	1.0
O13	0.217(7)	0.459(5)	0.269(13)	1.0
O14	0.285(5)	0.302(6)	0.498(9)	1.0
O15	0.141(4)	0.255(6)	0.323(11)	1.0
O16	0.280(4)	0.073(6)	0.510(11)	1.0
O17	0.228(5)	0.870(7)	0.384(9)	1.0
O18	0.113(4)	0.039(6)	0.449(11)	1.0
O19	0	0.211(9)	0.5	0.5
O20	0.249(38)	0.680(80)	0.175(95)	0.5
Extra-Framework Atom Sites	*x*	*y*	*z*	site occupancy factor, SOF
EFA_1	0	0.038	0	2.1
EFA_2	0.254	0.942	0.299	2.8
EFA_3	0.252	0.558	0.609	1.6
EFA_4	0.5	0.588	0.5	1.1
EFA_6	0.399	0.358	0.155	1.6
EFA_7	0.827	0.205	0.451	2.4
EFA_8	0.746	0.078	0.100	1.5
EFA_14	0.061	−0.397	0.323	1.6
EFA_16	0	−0.041	0.5	1.0
EFA_17	0	0.125	0	0.1
EFA_18	0.5	0.367	0.5	0.4

C atoms bonded to the Si atoms, indicating there are Si−CH_3 species between the layers of COE-1. This is also consistent with the results from ^{29}Si MAS NMR spectrum (see Figure 2a). Moreover, as indicated in Figure 3, the other weak signals at 9, 16, 50, and 67 ppm can be ascribed to the C atoms with different environments in the SDA of dimethyl dipropyl ammonium hydroxide.

The Ar isotherm of the IEZ material after calcination is shown in Figure 4a. The pore volume was determined as 0.17 cm^3/g, using the Horvath−Kawazoe method (0.18 cm^3/g based on MP method) for the COE-2 material with a pore diameter of >5 Å. From the N_2-adsorption/desorption experiments, the Langmuir surface area was calculated to be 540 m^2/g. Both Ar- and N_2-based measurements confirm the microporosity of the material with an extended pore diameter, compared to the regular zeolite

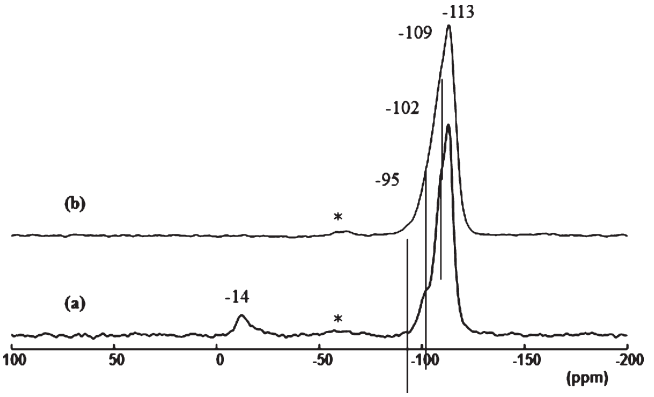

Figure 2. ^{29}Si MAS NMR spectra of IEZ-RRO before calcination showing the methyl-substituted siloxane bridge between the layers at (a) approximately −14 ppm and (b) after calcination with slighly enhanced intensity at approximately −95 ppm. Asterisk (*) denotes the spinning sidebands.

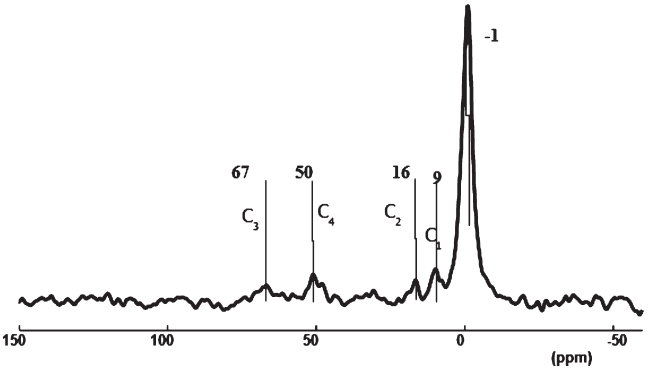

Figure 3. ^{1}H →^{13}C CP/MAS NMR spectrum of IEZ-RRO prior to calcination, showing the spectrum of the dimethyl-dipropylammonium cation serving as a structure-directing agent (SDA) (COE-1).

of the RRO framework type. The pore diameter also increased from values typical for 8-membered rings to intermediate pore size, which is typical for 10-membered rings or larger (5.3 Å diameter). The surface area of the IEZ-COE-2 materials is only slightly larger than that of RUB-41 (510 m^2/g.[15] This might be due to the fact that the interlayer expansion reaction leads to expanded interlayer spacings and increased pores, but, at the same time, also to extra hydroxyl groups at every interlayer linker group. This reduces the available space and is likely responsible for the moderate increase in surface area.

Sorption experiments with methane (CH_4) confirm the micropore volume and show uptake in the expected range (see Figure 4b). At a temperature of 298 K, CH_4 uptake amounts to 0.7 wt % at a final pressure of 900 Torr. The CH_4 uptake shows that the pore space of the expanded materials has not established repulsive forces for molecules such as CH_4.

Surprisingly, the PXRD experiments showed a diffraction diagram of a well-ordered, crystalline material with significant long-range periodicity. This is quite different from the experiments reported by Kuroda and co-workers on modification reactions using RUB-18 as a layered precursor,[27] and is also significantly different from the products introduced as the first examples of IEZ materials with the FER layer as a building unit.[40] Although

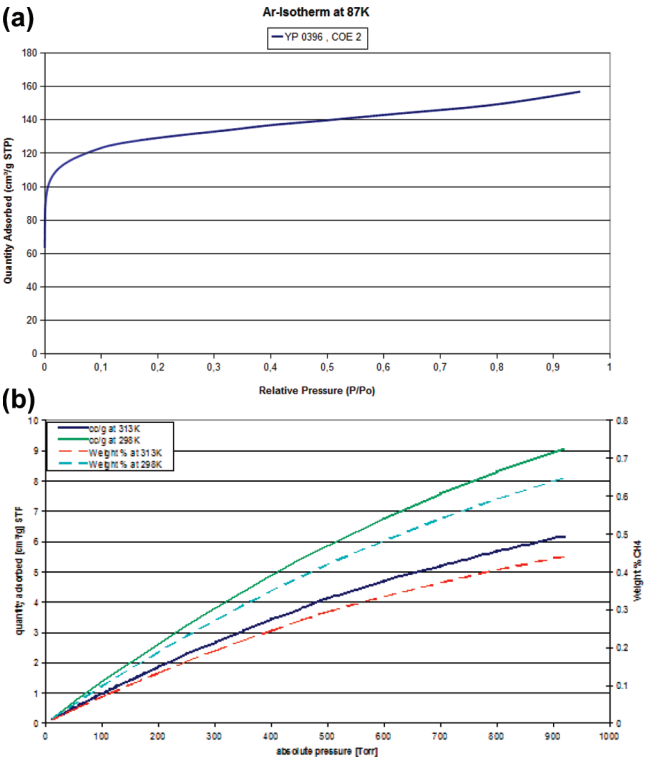

Figure 4. (a) Ar-adsorption isotherm of IEZ-RRO prior to calcination (COE-1), showing the porosity of the expanded material in the as-made state. (b) CH_4 isotherms as a function of pressure, measured at two different temperatures, showing the high affinity of the framework toward unpolar molecules.

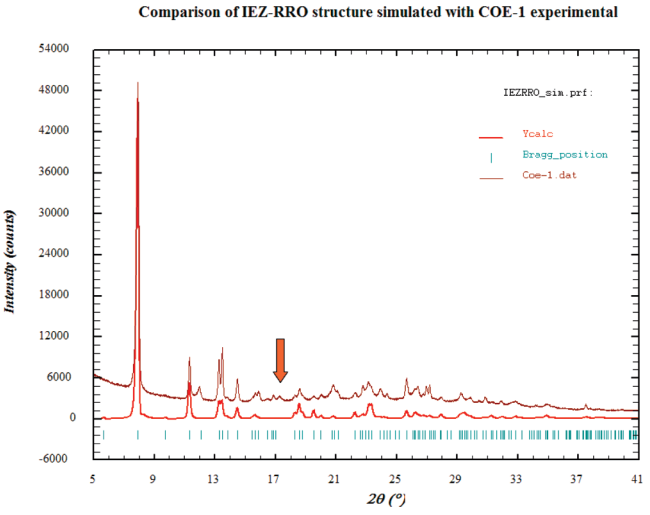

Figure 5. Comparison of X-ray diagram of the empty structure model derived from lattice parameters and after geometry optimization of the fractional coordinates with the experimental data. However, there is good agreement with regard to residual intensity, which must be matched by the refinement process.

transmission electron microscopy (TEM) images clearly demonstrated the expansion of silicate layers via the insertion of one tetrahedral unit, the PXRD diagram shows considerable line broadening, indicating significant structural incoherence. No structural study on these materials other than TEM images has

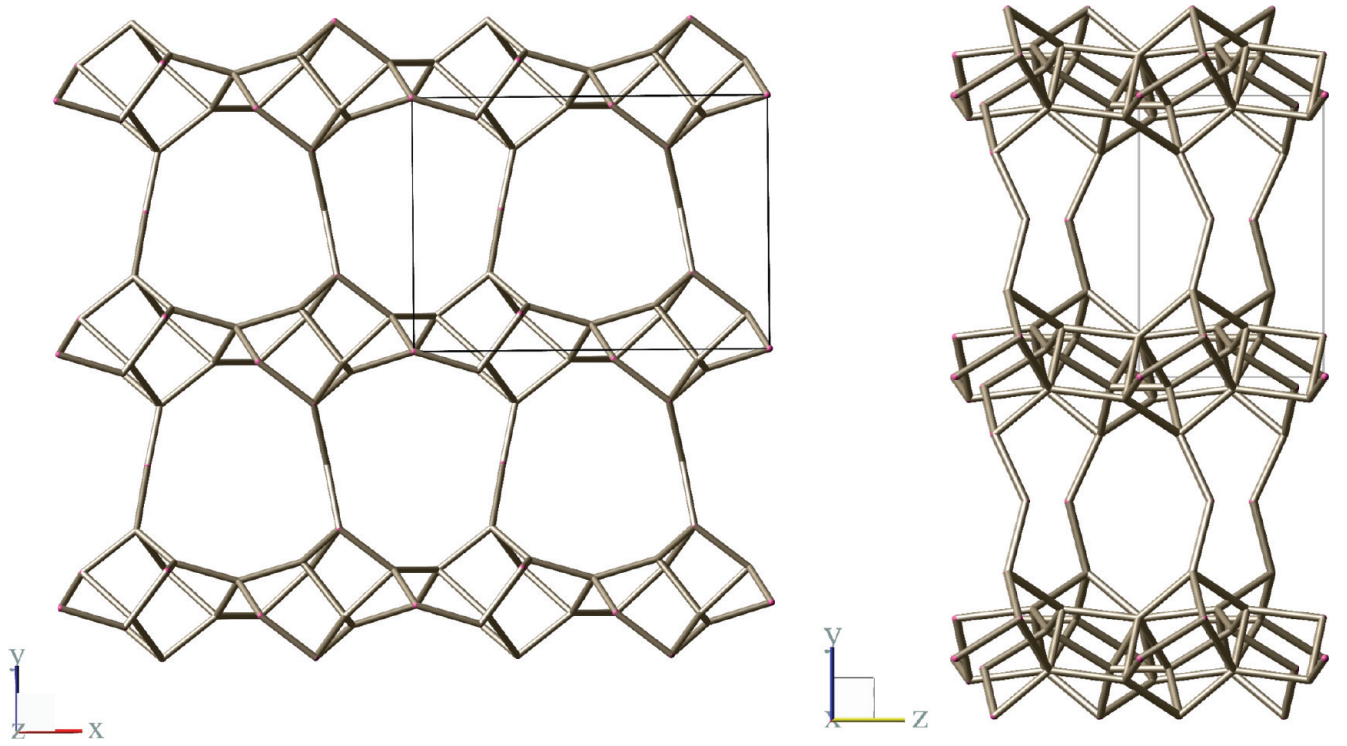

Figure 6. Skeletal model of the silicate framework of IEZ-RRO seen along the *z*-direction (left) and the *x*-direction (right). The projections show the increased pore diameter introduced by the siloxane bridges, which should be rather flexible, since they are only two-connected to the silicate framework.

been presented so far. For our material (COE-1), indexing the powder pattern with DICVOL[41] gave the following lattice parameters in space group *P*2: $a = 15.59$ Å, $b = 11.15$ Å, $c = 7.30$ Å, $\beta = 91.2°$ (for refined parameters, see Table 1). Using the same space group symmetry as that for the condensation product of RUB-39 (namely, zeolite RUB-41 (RRO topology)), the interlayer spacing is increased from 8.72 Å in RUB-41 to 11.15 Å for COE-1 (*b*-lattice parameter in both materials). The increase in lattice parameter *b*, by 2.43 Å, perfectly explains the insertion of one $[SiO_4]$ tetrahedron to link the two silicate layers. Choosing a new unit cell in the layer with angle β closer to 90° (91.2° for COE-1, instead of 114.2°), lattice parameter *a* of RUB-41 corresponds to lattice parameter *c* in COE-1 and *c* corresponds to *a*. Keeping the lattice parameters fixed, a structure model was derived and geometrically optimized using DLS. The fractional coordinates of the optimized structure model converged in the refinement to $R = 0.26\%$, indicating that a minimum energy fit for the framework geometry of COE-1 can be obtained, in agreement with the geometric boundary conditions typical for silicate crystal chemistry. Full details of the DLS analysis are summarized in Table 2. This DLS-optimized structure model for an "empty" IEZ-RRO, i.e., without residuals inside the pore system, then was used as the starting model for Rietveld analysis of the experimental powder diffraction data of as-made COE-1. As can be seen from Figure 5, simple visual inspection shows that there is a close resemblance between the two powder patterns.

Despite the considerable line broadening of the PXRD diagram, full-pattern Rietveld analysis clearly proved that the structure model of the interlayer expanded material is correct; however, because of the flexibility of the Q^2 linker group, strong periodicity has not been achieved. Including nonframework constituents, the refinement converged finally with $\chi^2 = 8.0$,

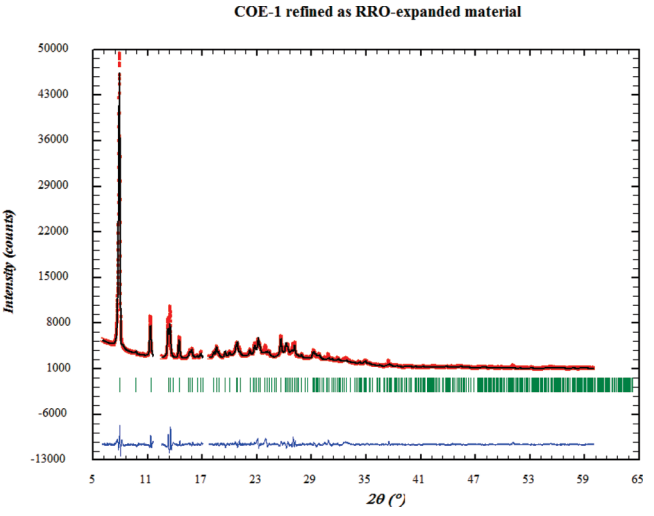

Figure 7. Results of the Rietveld refinement of the COE-1 PXRD data. Including nonframework scatterers, a good fit of the model can be achieved.

indicating that the fit of the simulated powder pattern on the experimental one is not perfect. The results of the refinement are summarized in Table 1 and Figures 6 and 7, with the final coordinates given in Table 5.

However, as can be seen from the extra intensity at 17.2° 2θ in the powder diagram (cf. Figure 5), which cannot be explained with the IEZ-RRO structure model, further structural modifications had to be considered. Since the expansion reaction is carried out under rather harsh hydrothermal conditions, stacking faults might occur, leading to a stacking-disordered silicate

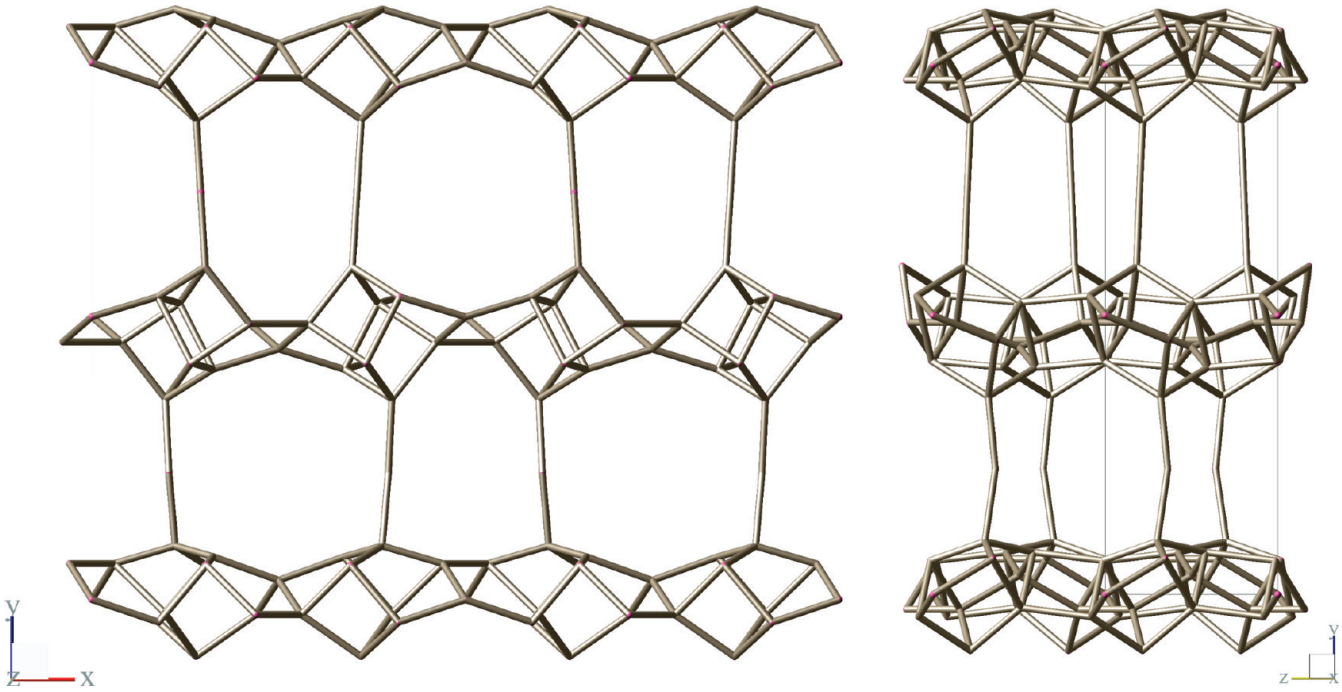

Figure 8. Structure model of IEZ-HEU, seen as projected along the *z*-direction (left) and *x*-direction (right), showing the alternative stacking sequence of materials with HEU layers. The structure model was derived from geometry-optimized coordinates.

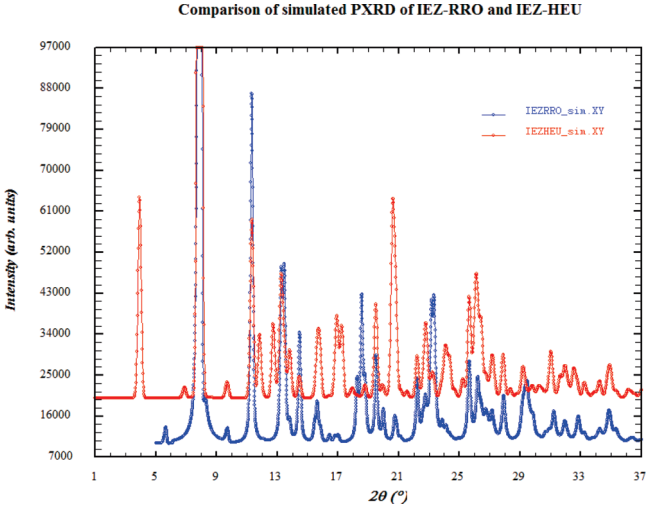

Figure 9. Comparison of the simulated powder diagrams of structure models of IEZ-RRO and IEZ- HEU. It is obvious that both materials have most peaks in common at the same 2θ values; however, there are distinct reflections for each of the polymorphs.

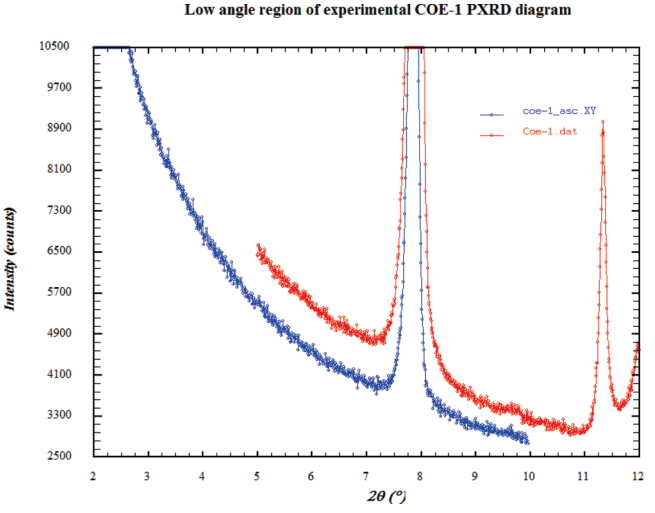

Figure 10. Extended PXRD dataset to low angle, confirming the nonexistence of pure IEZ-HEU material.

framework. This is also reflected in the considerable scatter of geometrical features of the silicate framework for particular [SiO_4] units (for example, the linking group). Si−Si distances are within the expected range (d(Si−Si) from 2.86(1) Å to 3.14(1) Å), O−O distances vary between 2.43(2) Å and 2.70(2) Å, and Si−O distances are between 1.48(2) Å and 1.79(2) Å, not considering the atoms involved with the linking group. Since the RRO framework type is the AA stacking variant of heulandite layers, the stacking sequence AB as in HEU-type materials for the interlayer expanded IEZ-HEU-framework model was derived, DLS-minimized (R-factor = 0.25%) (Table 4), and finally, again using the coordinates of the geometrically optimized structure, a simulated PXRD pattern was computed. The skeletal model of the silicate framework of IEZ-HEU is shown in Figure 8. In Figure 9, the simulated PXRD pattern of the two IEZ frameworks, IEZ-RRO and IEZ-HEU, are shown scaled to each other, using the strongest peak at 7.9° 2θ as reference and showing the strongest peak at the ∼10% level.

From the simulated powder pattern, it is obvious that IEZ-HEU would give rise to diffracted intensity in the 2θ region at ∼17° and might help us better explain the COE-1 powder pattern. However, IEZ-HEU has another unique extra peak at low angle (3.9° 2θ), which could be used to estimate the fraction of IEZ-HEU in the COE-1 material. However, extensive overexposure of

dx.doi.org/10.1021/cm103506q |*Chem. Mater.* 2011, 23, 2545–2554

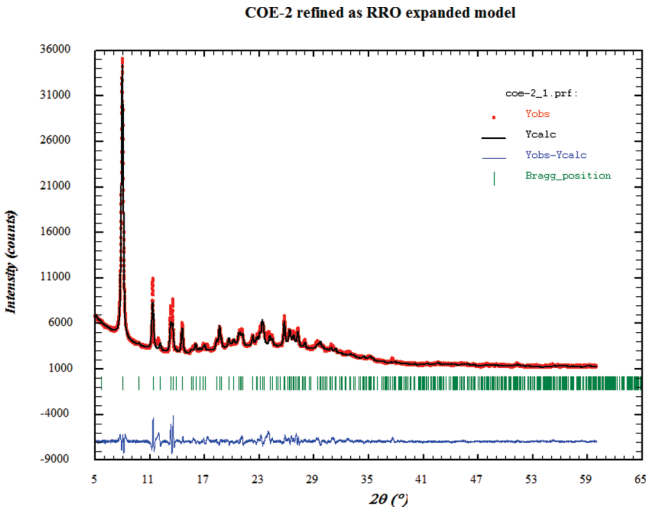

Figure 11. Rietveld refinement of COE-2, the calcined form of COE-1. A good quality fit is reached when scatterers on nonframework positions are included.

the low-angle region of the diffraction diagram did not show any indication of the low-angle peak in the PXRD diagram characteristic of IEZ-HEU (see Figure 10).

For the refinement of the structure of COE-2, which is obtained after thermal treatment of COE-1 at 550 °C overnight, similar analysis of the diffraction data was performed. Since, after calcination, the pore space is free of SDAs and the methyl groups that are attached to the bridging Si atom are oxidized to hydroxyl groups, the material more closely resembles the simulated powder pattern and is better suited for comparison. As already mentioned, the Rietveld analysis is not conclusive, since the low-angle peak at 3.9° 2θ was not observed in the experimental powder pattern. The final results of the Rietveld structure analysis are summarized in Table 1 and Figure 11. The structure plots of the silicate skeleton are similar to those of COE-1, which are represented in Figure 6.

In order to account for the influence of disorder on the powder diffraction diagram, DIFFaX calculations were carried out to simulate the powder patterns of intergrown IEZ-RRO/IEZ-HEU. For this purpose, calcined silica frameworks were used and intergrowth IEZ-RRO:IEZ-HEU ratios from 100:0 to 0:100 were computed, in steps of 10, assuming randomly stacked layers. The resulting simulated PXRD diagrams for IEZ-RRO/HEU stacking-disordered materials are presented in Figure 12. Comparing the PXRD diagrams, it is obvious that specific reflections change in intensity very sensitively, as a function of disorder, and can be used to evaluate the influence of disorder. Most surprisingly, the two low-angle peaks of IEZ-HEU are already very low in intensity after the addition of only 10% IEZ-RRO intergrowth. Therefore, despite their assignment to IEZ-HEU, they are not helpful for estimating the degree of IEZ-RRO/IEZ-HEU intergrowth. Similarly, the peak at ~15° 2θ in the diagram of IEZ-RRO quickly looses intensity after the addition of 10% IEZ-HEU intergrowth and almost disappears from 30% IEZ-HEU intergrowth onward. In fact, there are very sensitive shifts in intensity of distinct peaks, which indicate intergrowth of one form with the other, and there are many peaks that scale nicely with the degree of disorder over the entire range of admixture (e.g., the region between 15° and 24° 2θ).

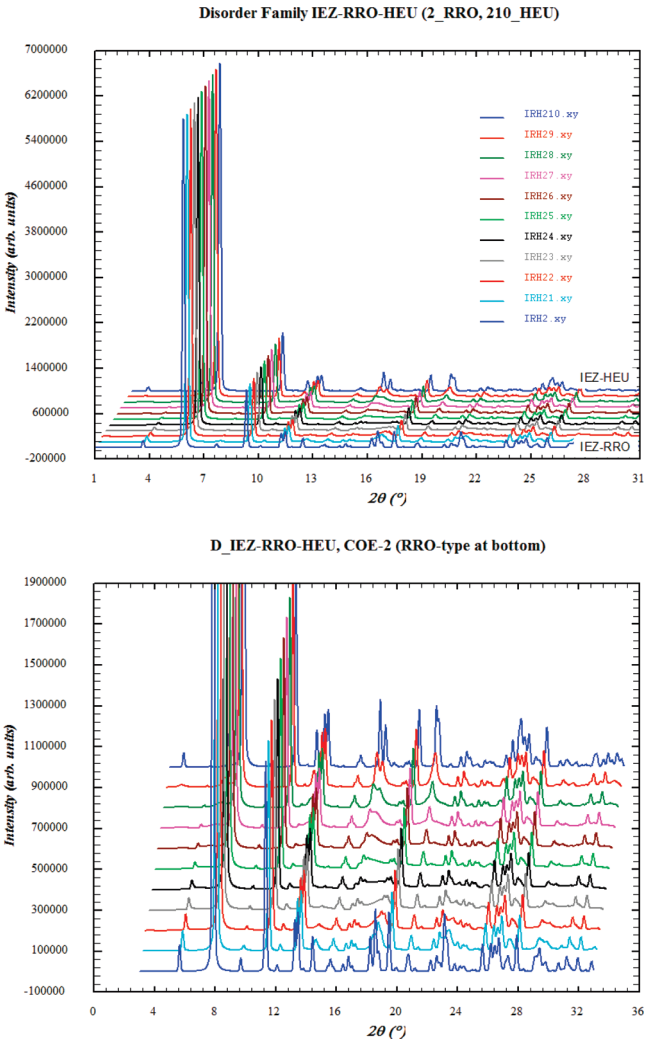

Figure 12. Simulation of the stacking disorder of IEZ-RRO/HEU materials shown in PXRD diagrams. The sequence of diagrams shows pure RRO-type stacking at the bottom of the sequence and pure HEU-type stacking at the top of the sequence. Intermediate diagrams show, in steps of 10%, the increased contribution of HEU stacking to the XRD diagram from bottom (10%) to the top (90%). (Top) Watch the steep decrease in intensity of the peak at ~12° 2θ when HEU stacking is added into the structure and the steep increase in intensity of the peak at ~3° 2θ when RRO-type stacking is running out. (Bottom) Enlarged view of the same diagrams of the disorder sequence, highlighting the sensible regions in the PXRD diagram; additional diffuse sections of the diffractogram can be observed.

Comparing now the experimental powder diagram of COE-2 (the calcined, layer-expanded material), it is immediately clear that a major fraction of the sample is pure IEZ-RRO, since the sharp peak at ~15° 2θ shows no peak broadening, i.e., there is no considerable amount of intergrowth of IEZ-HEU. On the other hand, since there is no intensity at low angles (3.9° 2θ), pure IEZ-HEU is very unlikely, and at least 10% IEZ-RRO intergrowth should be present. From the analysis of the experimental powder diagram and the comparison with the simulated powder diagrams of the disorder series, it is concluded that the COE-1 and COE-2 materials are composed of two framework realizations, one being pure IEZ-RRO and the other being intergrown IEZ-1RRO/9HEU, in the mass ratio of 2:1. Figure 13 shows the

dx.doi.org/10.1021/cm103506q |*Chem. Mater.* 2011, 23, 2545–2554

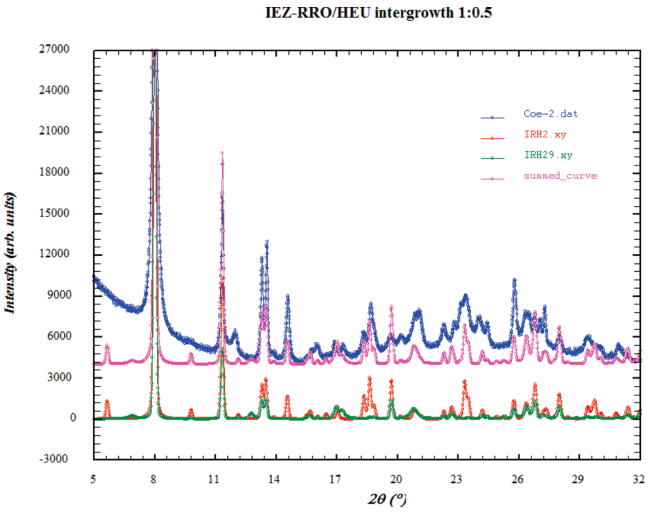

Figure 13. Comparison of the PXRD data of COE-2 with the sum-diagram obtained from structure models of material with two disorder probabilities. Comparison with the experimental diagram shows that peak positions in the experimental diagram can be accounted for with allowed peak positions in diagrams of the simulation of the disordered material. Still, since the model does not contain nonframework constituents, peak intensities of the model do not always match the intensities of the experimental pattern.

simulated powder diagram of the composite material, together with the experimental powder pattern. Because of the complexity of the problem, no refinement of the structure model against the experimental data is possible, especially since nonframework constituents are still present inside the pore system and are not considered in the simulations.

From the results of the structure analysis, a conception about the mechanism of formation of the interlayer-expanded material can be gained. On one hand, the regular RRO-stacking sequence indicates that an insertion of the silylating agent DCDMS between silicate layers takes place and, after fixing the orientation of neighboring layers at a minimum of two sites, the relative orientation is preset and should continue in a zipperlike manner without creating further defects (see Figure 14). However, HEU stacking requires a new alignment of layers, with respect to the layer stacking in the RUB-39 starting material. The simplest mechanism of formation of HEU-like stacking of silicate layers involves delamination of RUB-39 first and, in a second step, reassembly of layers during hydrothermal treatment. The silylating agent then can access the surface silanol groups and link it in an alternative HEU-type fashion. Similar reactions have already been described for the synthesis of Ti-MCM-22,[23−26] where the layered precursor was delaminated for the introduction of Ti on T-sites and reassembled to form the three-dimensional (3D) zeolite framework of Ti-MCM-22. Since the silylation reaction is carried out under strongly acidic conditions and is followed by a hydrothermal treatment at $T \approx 170$ °C, partial delamination of the layered precursor RUB-39 should occur, as a competitive process to the DCDMS insertion. Information that supports the reassembly of delaminated RUB-39 comes from the DLS refinement of the two-interlayer-expanded framework. Since the distance optimization is comparable to an energy minimization, the R-factor of the refinement can be used to evaluate relative stabilities. IEZ-HEU refines to a slightly lower R-factor (0.25%) than IEZ-RRO (0.33%), favoring reassembly of the IEZ-HEU framework after delamination. This might explain the high percentage of HEU stacking in one of the

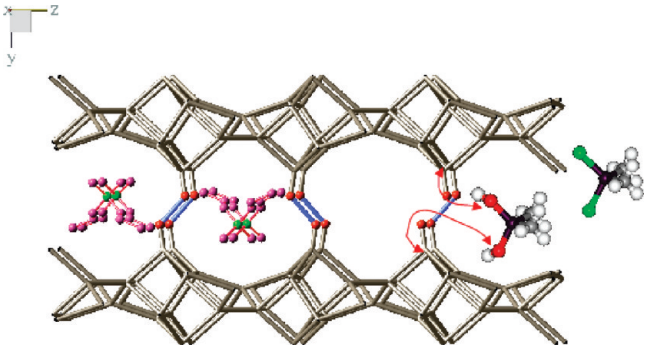

Figure 14. Visualization of the insertion reaction of dichloro-dimethylsilane (green) after hydrolysis to dihydroxo-dimethylsilane (red) between RUB-39 silicate layers for interlayer expansion, leading to pure IEZ-RRO material. In the case of delamination of the parent material, IEZ-HEU stacking also can occur.

expanded materials. Experiments of purposeful delamination and reassembly should prove this hypothesis.

CONCLUSIONS

Interlayer expansion of RUB-39 with DCDMS leads to new microporous materials with tunable pore geometry and pore openings. The study shows that the reaction product is quite homogeneous, particularly as far as pore space is concerned. This is also demonstrated in nitrogen and methane sorption isotherm measurements, showing the increased surface area and pore diameter of the expanded material. The crystallinity of the material (i.e., the strong periodicity of the silicate framework) suffers from the stacking disorder introduced during the expansion reaction and the rather-high flexibility of the linking dimethylsilane group. Simulation of powder X-ray diagrams modeling the stacking disorder of layers indicated that two modes of interlayer expansion have occurred, leading to a mixture of two, very related materials. Still, Rietveld analysis of the powder X-ray diffraction (PXRD) pattern using the IEZ-RRO framework model very nicely describes the structural features of the material and shows the homogeneity of the three-dimensional (3D) bonding network. Structure analysis also shows that the pore geometry of the different stacking sequences is almost identical and should not influence its typical catalytic or sorption properties.

The potential of the interlayer expansion method applied to layer-silicate precursors lies in the general applicability, as demonstrated here for the RUB-39 family of materials. More structural families should become accessible in the near future. Different silylating agents as linker groups should lead to larger pore openings. Replacing the methyl group with other, functional groups at the linker position should add new functionalities accessible in the void space for chemical, catalytic reactions. The particular benefit of this method is the fine-tunability of pore space and geometry, together with added functional groups.

AUTHOR INFORMATION

Corresponding Author

*E-mail: hermann.gies@rub.de.

ACKNOWLEDGMENT

This work was performed under the framework of the INCOE (International Network of Centers of Excellence) project coordinated by BASF SE.

REFERENCES

(1) Dyer, A. *Stud. Surf. Sci. Catal.* **2005**, *157*, 181.
(2) Corma, A.; Martinez, A. *Stud. Surf. Sci. Catal.* **2005**, *157*, 337.
(3) Hafner, J.; Benco, L.; Bucko, T. *Top. Catal.* **2006**, *37*, 41.
(4) Yilmaz, B.; Müller, U. *Top. Catal.* **2009**, *52*, 888.
(5) Chen, H. B.; Johnson, J. K.; Sholl, D. S. *J. Phys. Chem. B* **2006**, *110*, 1971.
(6) Davis, R. J. *J. Catal.* **2003**, *216*, 396.
(7) Thomas, J. M.; Rajac, R. *Catal. Today* **2006**, *117*, 22.
(8) Johnson, T. *Plat. Met. Rev.* **2008**, *52*, 23.
(9) Baek, S.; Kim, J.; Ihm, S. *Stud. Surf. Sci. Catal.* **2004**, *154*, 2458.
(10) McCusker, L. B.; Baerlocher, Chr. *Database of Zeolite Structures*, http://www.izastructure.org/databases.
(11) Bellussi, G.; Pollesel, P. *Surf. Sci. Technol. Catal.* **2005**, *158*, 1201.
(12) Ishii, R.; Ikeda, T.; Itoh, T.; Ebina, T.; Yokoyama, T.; Hanaoka, T.; Mizukami, F. *J. Mater. Chem.* **2006**, *16*, 4035.
(13) Millini, R.; Carluccio, L. C.; Carati, A.; Bellussi, G.; Perego, C.; Cruciani, G.; Zanardi, S. *Microporous Mesoporous Mater.* **2004**, *74*, 59.
(14) Rollmann, L. D.; Schlenker, J. L.; Lawton, S. L.; Kennedy, C. L.; Kennedy, G. J. *Microporous Mesoporous Mater.* **2002**, *53*, 179.
(15) Wang, Y. X.; Gies, H.; Marler, B.; Müller, U. *Chem. Mater.* **2005**, *17*, 43.
(16) Marler, B.; Stroter, N.; Gies, H. *Microporous Mesoporous Mater.* **2005**, *83*, 201.
(17) Marler, B.; Camblor, M. A.; Gies, H. *Microporous Mesoporous Mater.* **2006**, *90*, 87.
(18) Hida, E.; Oumi, Y; Ikeda, T.; *J. Ceram. Soc. Jpn.* **2005**, *113*, 424.
(19) Yilmaz, B.; Müller, U.; Tijsebaert, B.; *Chem. Commun.* **2011**, *47*, 1812.
(20) Corma, A.; Diaz, U.; Fornes, V.; *Chem. Commun.* **1999**, *9*, 779.
(21) Roth, W. J.; Vartuli, J. C. *Stud. Surf. Sci. Catal.* **2002**, *141*, 273.
(22) Inagaki, S.; Kamino, K.; Kikuchi, E.; Matsukata, M. *Appl. Catal., A* **2007**, *318*, 22.
(23) Wu, P.; Tatsumi, T. *J. Catal.* **2003**, *214*, 317.
(24) Wu, P.; Fan, W.; Nuntasri, D.; Tatsumi, T. *Stud. Surf. Sci. Catal.* **2004**, *154*, 2581.
(25) Wu, P.; Nuntasri, D.; Ruan, J. F.; *J. Phys. Chem. B* **2004**, *108*, 19126.
(26) Wu, P.; Tatsumi, T. *Catal. Surv. Asia* **2004**, *8*, 137.
(27) Inagaki, S.; Yokoi, T.; Kubota, Y.; Tatsumi, T. *Chem. Commun.* **2007**, *48*, 5188.
(28) Wu, P.; Ruan, J.; Wang, L.; Wu, L. L.; Wang, Y.; Liu, Y.; Fan, W; He, M. Y.; Terasaki, O.; Tatsumi, T. *J. Am. Chem. Soc.* **2008**, *130*, 8178.
(29) Inagaki, S.; Tatsumi, T. *Chem. Commun.* **2009**, *18*, 2583.
(30) Mochizuki, D.; Shimojima, A.; Imagawa, T.; Kuroda, K. *J. Am. Chem. Soc.* **2005**, *127*, 7183.
(31) Mochizuki, D.; Kowata, S.; Kuroda, K. *Chem. Mater.* **2006**, *18*, 5223.
(32) Mochizuki, D.; Kuroda, K. *New J. Chem.* **2006**, *30*, 277.
(33) Wang, Y. X.; Gies, H.; Lin, J. H. *Chem. Mater.* **2007**, *19*, 4181.
(34) Tijsebaert, B.; Varszegi, C.; Gies, H.; Xiao, F. S.; Bao, X. H.; Tatsumi, T.; Müller, U.; De Vos, D. *Chem. Commun.* **2008**, *21*, 2480.
(35) Tijsebaert, B.; Yilmaz, B.; Müller, U.; Gies, H.; Zhang, W.; Bao, X.; Xiao, F.; Tatsumi, T.; De Vos, D. *J. Catal.* **2011**, *278*, 246.
(36) Baerlocher, Ch.; Hepp, A.; Meier, W. M. *DLS-76: A Program for the Simulation of Crystal Structures by Geometric Refinement*; Institute of Crystallography and Petrography, ETH: Zürich, Switzerland, 1976.
(37) Rodriguez-Carvajal, J. *Physica B* **1993**, *192*, 55.
(38) Rodriguez-Carvajal, J. *FullProf Suite Homepage*; http://www.ill.eu/sites/fullprof/.
(39) Treacy, M. M. J.; Newsam, J. M.; Deem, M. W. *R. Soc. Proc. London, A* **1991**, *433*, 499.
(40) Wu, P.; Ruan, J.; Wang, L.; Wu, L.; Wang, Y.; Liu, Y.; Fan, W.; He, M.; Terasaki, O.; Tatsumi, T. *J. Am. Chem. Soc.* **2008**, *130*, 8178.
(41) Louer, D.; Boultif, A. *Z. Kristallogr.* **2006**, No. Suppl. 23, 225.